Femtosecond-rate space-to-time conversion

Dan Marom,* Dmitriy Panasenko, Pang-Chen Sun, and Yeshaiahu Fainman

Department of Electrical and Computer Engineering, University of California, San Diego, 9500 Gilman Drive, La Jolla, California 92093-0407

Received June 12, 2000

A real-time spatial–temporal processor based on cascaded nonlinearities converts space-domain images to time-domain waveforms by the interaction of spectrally decomposed ultrashort pulses and spatially Fourier-transformed images carried by quasi-monochromatic light waves. We use four-wave mixing, achieved by cascaded second-order nonlinearities with type II noncollinear phase matching, for femtosecond-rate processing. We present a detailed analysis of the nonlinear mixing process with waves containing wide temporal and angular bandwidths. The wide bandwidths give rise to phase-mismatch terms in each process of the cascade. We define a complex spatial–temporal filter to characterize the effects of the phase-mismatch terms, modeling the deviations from the ideal system response. New experimental results that support our findings are presented. © 2000 Optical Society of America [S0740-3224(00)01410-7]

OCIS codes: 070.1170, 320.5540, 190.7110, 190.4380.

1. INTRODUCTION

Methods for ultrafast optical waveform synthesis (also referred to as pulse shaping) have been investigated for diverse applications in the natural sciences and engineering. Reviews of various pulse-shaping techniques can be found in Refs. 1 and 2. Based on linear-system theory, filtering the temporal-frequency components of an ultrashort optical pulse results in high-resolution waveform synthesis. The filtering can be achieved by spatially dispersing the frequency components in a spectral processing device (SPD), a free-space optical setup consisting of diffraction gratings and lenses, and inserting a spatial mask with the encoded amplitude and phase information. After the spectral decomposition wave[3] (SDW) has been filtered by the spatial mask, the frequency components are recomposed in the SPD to generate the synthesized temporal waveform. Early pulse-shaping experiments used prefabricated masks to filter the SDW,[4] which later were replaced by active-filtering devices such as spatial light modulators[5] and acousto-optic modulators.[6] This approach may not yield an adequate time response for adaptive control of the synthesized waveform needed for some applications, as it is limited by computation time, signal propagation delay, and modulator response time. Additionally, most modulators operate with either phase or amplitude modulation, requiring a complicated cascade of two devices for complete complex-amplitude filtering.[7] An alternative approach for generating the spectral filter uses *in situ* optical holographic recording of the interference of the spatial Fourier transform (FT) of a spatial image and a reference point source.[8,9] The recorded spatial-frequency information serves as a spectral filter for the SDW of an incident ultrashort reference pulse. The synthesized waveform is correlated to the spatial image used in the recording, resulting in a space-to-time converted image. This approach can be interpreted as a four-wave mixing process between two waves carrying spatial FT information and two SDW's with the temporal FT information, resulting in the exchange of information between the spatial and temporal channels. The holographic recording medium's characteristics determine the performance of the information exchange between the four interacting waves. For example, using holographic film will require a long recording and processing time. Thick holograms formed in bulk photorefractive crystals yield high diffraction efficiency but also require a long recording time owing to slow electron mobility essential in buildup of a space-charge field[9] (from tens of microseconds to several minutes). Multiple-quantum-well (MQW) semiconductor photorefractives can perform holographic recording with a microsecond response time yet result in low diffraction efficiency owing to the short interaction length.[10,11]

For compatibility with the requirements of ultrafast applications such as high-speed optical communication with ultrashort pulses and quantum control of atomic and molecular vibrational states, the synthesized waveform must be updated, or modulated, at high rates with both amplitude and phase information. Such a femtosecond-rate response time can be provided only by parametric processes that involve bound-electron nonlinearities. Our space-to-time conversion scheme, first reported in Ref. 12, exchanges the information from a spatial image to a temporal waveform by a four-wave mixing process in a $\chi^{(2)}$ nonlinear crystal. The cascaded second-order nonlinearity (CSN) arrangement we are utilizing consists of a frequency-sum generation process followed by a frequency-difference generation process that satisfies the type II noncollinear phase-matching condition.[13] The nonlinear wave mixing occurs in the Fourier domain of the temporal and spatial channels (see Fig. 1). The frequency-sum process mixes the SDW of the input ultrashort pulse and the spatial FT of the spatial-image information illuminated with a quasi-monochromatic plane wave. The resultant intermediate wave is determined by the product of the complex amplitudes of the temporal and spatial FT fields. The cascaded frequency-difference process mixes the intermediate wave with the spatial FT of a point source illuminated by the same quasi-

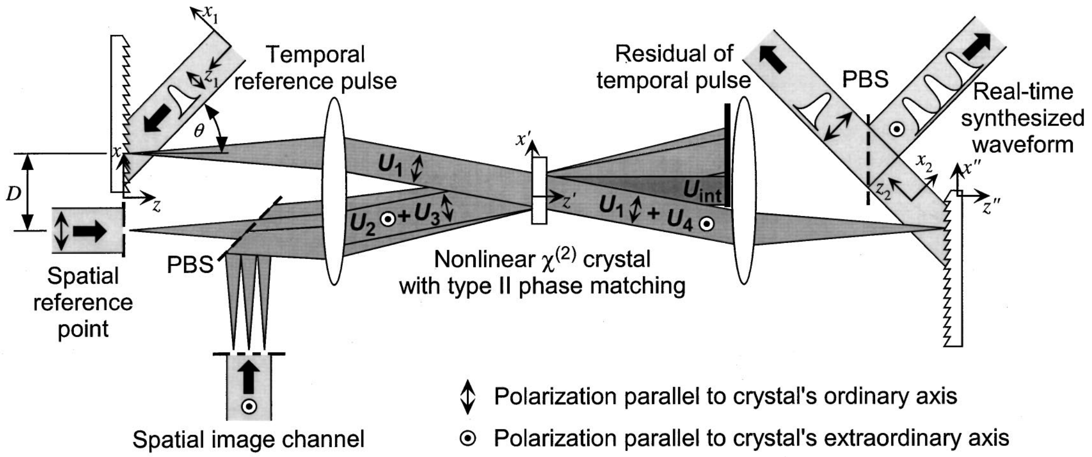

Fig. 1. Femtosecond-rate space-to-time conversion setup based on nonlinear wave mixing with noncollinear type II cascaded second-order nonlinearities in the Fourier-domain plane of the temporal and spatial channels. A frequency-sum process between waves U_1 and U_2 gives rise to the wave $U_{\rm int}$. A frequency-difference process between the waves $U_{\rm int}$ and U_3 generates the desired output wave U_4.

monochromatic plane wave. The second spatial wave contains no information, in either the space or the time domain, and its function is to downconvert the carrier frequency of the intermediate wave generated by the first nonlinear process. The resultant field in the CSN process is the filtered SDW, which is recomposed to yield the synthesized output temporal waveform.

In this paper we describe and analyze in depth the space-to-time conversion process employing CSN, achieving a femtosecond response time and high conversion efficiency. In contrast to our initial analysis in the time domain,[12] a temporal-frequency-domain analysis is presented in Section 2, in which we develop the expression for the synthesized temporal waveform under the assumption of an ideal CSN process with perfect phase matching. In Section 3 we investigate the effects of the phase-mismatch terms in the cascaded processes and characterize them with a complex spatial–temporal transfer function. The derivation of the phase-mismatch terms' dependence on the temporal- and spatial-frequency bandwidths is deferred to the appendix. Experimental results verifying the findings of our analysis are presented in Section 4, illustrating the ability to convert both amplitude and phase information with this technique. We conclude with a summary and discussion in Section 5.

2. ANALYSIS OF THE SPACE-TO-TIME CONVERTER

The nonlinear interaction between the SDW of the input ultrashort pulse and the quasi-monochromatic waves at the Fourier plane of the optical setup is analyzed in this section under the following assumptions: (i) The nonlinear wave-mixing process is weak, such that the amplitude of the generated wave is proportional to the product of the complex amplitudes of the mixed waves. (ii) The interacting waves are phase matched for all temporal frequencies contained in the bandwidth of the short pulse and spatial frequencies of the spatial image. We defer the justification and discussion on the validity of this last assumption to Section 3, in which a complex filtering response function is introduced to characterize the effect of phase mismatch on the conversion process. Since the space-to-time conversion occurs for one-dimensional spatial signals, the y-axis information is omitted. In the following, we first analyze the input temporal- and spatial-information channels, followed by an analysis of the CSN wave-mixing process giving rise to the synthesized temporal waveform.

A. Input Optical Channels

An ultrashort optical pulse, with a temporal envelope waveform of $p(t)$, is utilized at the input temporal channel of the SPD. The pulse is propagating in free space toward a diffraction grating, at an angle θ relative to the grating normal (see Fig. 1). The input ultrashort pulse is characterized in the propagating pulse's coordinate system (x_1, z_1) as

$$E_{\rm pulse}(x_1, z_1;\, t) = w_1(x_1) p\left(t - t_0 - \frac{z_1}{c}\right) \times \exp\left[j\left(\frac{\omega_0}{c} z_1 - \omega_0 t\right)\right], \qquad (1)$$

where $w_1(\ )$ defines the transversal field distribution or the spatial mode of the pulse, c is the speed of light in vacuum, ω_0 is the center optical frequency, and t_0 is an arbitrary time reference. The pulse is propagating in the z_1 direction at a group velocity and a phase velocity of the speed of light. We assume the spatial mode size of the pulse is sufficiently large to ignore diffraction effects in the region of interest near the grating for the representation of Eq. (1) to be valid.

Since we are assuming that the nonlinear wave mixing of the space-to-time converter operates in the linear regime, the signal analysis may be performed in the temporal-frequency domain. We Fourier transform (FT) Eq. (1) to perform a temporal-frequency decomposition of the short pulse, yielding

$$\tilde{E}_{\rm pulse}(x_1, z_1;\, \omega) = w_1(x_1) \exp\left(j \frac{\omega}{c} z_1\right) \tilde{p}(\omega - \omega_0) \times \exp[j(\omega - \omega_0) t_0], \qquad (2)$$

where the tilde overscript denotes a FT, e.g., $\tilde{p}(\omega) = \int p(t)\exp(j\omega t)\mathrm{d}t$. We perform a rotation of the coordinate system from (x_1, z_1) to (x, z) for compatibility with the coordinate system of the SPD, yielding

$$\tilde{E}_{\text{pulse}}(x, z;\ \omega) = w_1(-z\sin\theta + x\cos\theta) \times \exp\left[j\frac{\omega}{c}(-z\cos\theta - x\sin\theta)\right] \times \tilde{p}(\omega - \omega_0)\exp[j(\omega - \omega_0)t_0]. \tag{3}$$

To find the incident field on the input grating of the SPD, the field of Eq. (3) is evaluated at $z = 0$. The effect of the grating diffraction can be modeled by adding the grating momentum, k_g, in the x direction to the k vector that characterizes the propagation direction of the wave, resulting in

$$\tilde{E}_{\text{input}}(x, 0;\ \omega) = w_1(x\cos\theta)\exp\left[-j\left(\frac{\omega}{c}\sin\theta - k_g\right)x\right] \times \tilde{p}(\omega - \omega_0)\exp[j(\omega - \omega_0)t_0]. \tag{4}$$

The grating momentum, k_g, and the incidence angle, θ, are chosen such that the center frequency ω_0 will diffract in the direction of the optical axis of the system. Setting $\omega_0 \sin\theta/c = k_g$ and substituting the grating's k vector, $k_g = 2\pi/\Lambda$, where Λ is the grating period, yields $\sin\theta = \lambda_0/\Lambda \equiv \alpha$, where λ_0 is the center wavelength. To further simplify the notation, we define a new spatial-aperture function such that $w(x) = w_1(x\cos\theta)$. Without loss of generality we also shift the input aperture of the beam from the optical axis of the system by $D/2$. This is done to satisfy the noncollinear beam-propagation requirement in the Fourier plane of the SPD for phase matching in the CSN process. The input temporal-channel field to the optical processor, u_{tc1}, is therefore characterized by

$$\tilde{u}_{\text{tc1}}(x;\ \omega) = w\left(x - \frac{D}{2}\right)\exp\left[-j(\omega - \omega_0)\frac{\alpha x}{c}\right] \times \tilde{p}(\omega - \omega_0)\exp[j(\omega - \omega_0)t_0]. \tag{5}$$

We may inverse FT Eq. (5) to generate the input signal in the time domain, yielding

$$u_{\text{tc1}}(x;\ t) = w\left(x - \frac{D}{2}\right)p\left(t - t_0 + \frac{\alpha x}{c}\right)\exp(-j\omega_0 t). \tag{6}$$

Equation (6) describes the short pulse scanning across the fixed aperture at a velocity of $-c/\alpha$ in the x direction. For convenience we may wish to set the time-delay parameter such that the traveling pulse is at the center of the aperture at $t = 0$. This is achieved by setting $t_0 = \alpha D/2c$.

The temporal-channel field of Eq. (5) is spatially Fourier transformed by a lens of focal length f, yielding the SDW U_1 of the short pulse,

$$U_1(x';\ \omega) = \tilde{p}(\omega - \omega_0)\exp[j(\omega - \omega_0)t_0] \times \int_{-\infty}^{\infty} w\left(x - \frac{D}{2}\right)\exp\left[-j(\omega - \omega_0)\frac{\alpha x}{c}\right] \times \exp\left(-j2\pi\frac{xx'}{\lambda f}\right)\mathrm{d}x, \tag{7}$$

where we defer solving this Fourier integral to the nonlinear wave-mixing analysis of Section 3. The two spatial channels, one containing the encoding information and the second a point source, are modeled next.

A mask containing spatial-domain information is placed in the input plane of the processor, alongside the diffraction grating used for the input temporal channel. The mask is shifted from the optical axis by $-D/2$ to satisfy the requirement of noncollinear beam propagation in the Fourier plane of the SPD. The information mask of the spatial channel is illuminated with a quasi-monochromatic light source at center frequency ω_1. The first input spatial channel of the processor, u_{sc1}, can be expressed as

$$u_{\text{sc1}}(x,\ z = 0;\ t) = m\left(x + \frac{D}{2}\right)\exp(-j\omega_1 t), \tag{8}$$

where $m(x)$ is the spatial-information mask. The first input spatial-channel field is spatially Fourier transformed by the lens, yielding the field U_2, which we express in the temporal-frequency domain by taking the temporal FT, generating

$$U_2(x';\ \omega) = \delta(\omega - \omega_1)\int_{-\infty}^{\infty} m\left(x + \frac{D}{2}\right) \times \exp\left(-j2\pi\frac{xx'}{\lambda_1 f}\right)\mathrm{d}x, \tag{9}$$

where $\delta(\ )$ is the Dirac delta function. The spatial wave contains no temporal-frequency bandwidth owing to our illumination with a quasi-monochromatic light source.

The second spatial channel consists of a point source at the input plane that is illuminated by the same quasi-monochromatic light source as the first spatial channel. The point source is shifted from the optical axis by $-D/2$, as the first spatial channel has been. A polarization-selective beam splitter (see PBS in Fig. 1) is used for efficient superposition of the two spatial channels necessary for the wave-mixing process. The second input spatial-channel field to the processor, u_{sc2}, can be expressed as

$$u_{\text{sc2}}(x;\ t) = \delta\left(x + \frac{D}{2}\right)\exp(-j\omega_1 t). \tag{10}$$

The second input spatial-channel field is also spatially Fourier transformed by the lens, yielding the field in the Fourier plane U_3, expressed in the temporal-frequency domain as

$$U_3(x';\ \omega) = \delta(\omega - \omega_1)\int_{-\infty}^{\infty}\delta\left(x + \frac{D}{2}\right) \times \exp\left(-j2\pi\frac{xx'}{\lambda_1 f}\right)\mathrm{d}x. \tag{11}$$

We next examine the space–time conversion process by nonlinear wave mixing the three waves defined in Eqs. (7), (9), and (11).

B. Four-Wave Mixing by the Cascaded Second-Order Nonlinearity Process

A nonlinear crystal exhibiting a large nonlinear susceptibility $\chi^{(2)}$ is placed at the Fourier plane of the SPD (see Fig. 1). The two optical waves, U_1 and U_2, from the input temporal channel and the first spatial channel interact within the crystal, giving rise to an intermediate wave U_{int} in a frequency-sum process. The type II noncollinear phase-matching condition is satisfied by (i) adjusting the polarization directions of the temporal and spatial channels to coincide with the crystal's ordinary and extraordinary directions, respectively, and (ii) setting the interacting input waves to propagate noncollinearly. The second condition is satisfied by the spatial separation of the input channels, resulting in a propagation-direction-difference angle of D/f between U_1 and U_2. The complex amplitude of the generated intermediate wave is proportional to the nonlinear polarization arising from the two fundamental waves, yielding

$$U_{\mathrm{int}}(x';\ \omega) \propto \chi_{\mathrm{eff}}^{(2)}\int_{-\infty}^{\infty}U_1(x';\ \omega - \Omega)U_2(x';\ \Omega)\mathrm{d}\Omega = \chi_{\mathrm{eff}}^{(2)}U_1(x';\ \omega - \omega_1)U_2(x';\ \omega_1), \tag{12}$$

where $\chi_{\mathrm{eff}}^{(2)}$ is the effective nonlinear-susceptibility coefficient at the propagation directions of the interacting waves, and we assume it to be independent of ω in the temporal-frequency bandwidth of interest. The convolution integral describing the nonlinear polarization is trivial to solve since U_2 has no temporal-frequency bandwidth. The intermediate wave is therefore shifted up in frequency by ω_1, such that U_{int} is oscillating at a center frequency of $\omega_0 + \omega_1$ and is polarized in the extraordinary direction owing to the type II interaction.

Next, we consider the interaction of the third wave U_3 with the other waves in the nonlinear crystal. Since the crystal exhibits type II phase matching, there is no interaction between the wave from the temporal channel U_1 and the wave from the second spatial channel U_3, as they are both polarized in the ordinary-axis direction of the crystal. The collinear waves from the two spatial channels produce a second-harmonic wave, but it is of no interest for our study of the spatial–temporal processor. The signal of interest is generated from the interaction of the wave from the second spatial channel U_3 and the intermediate wave U_{int} generated in the frequency-sum process. These two waves are orthogonally polarized and satisfy the noncollinear phase-matching condition for a frequency-difference generation process. The noncollinear phase-matching condition is automatically satisfied because U_2 and U_3 have the same optical frequency and copropagate. The interaction of U_3 and U_{int} gives rise to a fourth wave U_4 at the output of the nonlinear crystal, which is our signal of interest, given by

$$\begin{aligned}U_4(x';\ \omega) &\propto \chi_{\mathrm{eff}}^{(2)}\int_{-\infty}^{\infty}U_{\mathrm{int}}(x';\ \omega + \Omega)U_3^*(x';\ \Omega)\mathrm{d}\Omega\\ &= \chi_{\mathrm{eff}}^{(2)}U_{\mathrm{int}}(x';\ \omega + \omega_1)U_3^*(x';\ \omega_1)\\ &= (\chi_{\mathrm{eff}}^{(2)})^2U_1(x';\ \omega)U_2(x';\ \omega_1)U_3^*(x';\ \omega_1).\end{aligned} \tag{13}$$

The nonlinear polarization has the form of a correlation integral in the frequency-difference process. This integral is again trivial to solve, as the second spatial channel is also quasimonochromatic. The output wave is equivalent to a four-wave mixing process achieved by cascaded second-order nonlinearities. The resultant wave, U_4, is the SDW of the synthesized waveform with center frequency ω_0, generated by filtering the input SDW U_1 by a spatially modulated wave. It is copropagating with U_1 and polarized in the extraordinary direction (as U_{int} is extraordinary and U_3 is ordinary). Polarization optics may be used to separate the copropagating waves U_1 and U_4 (see Fig. 1).

The generated field U_4 is spatially Fourier transformed by a lens of focal length f, yielding the optical field on the output diffraction grating, given by

$$\begin{aligned}u_{tc2}(x'';\ \omega) &= \int_{x'}U_4(x';\ \omega)\exp\left(-j\frac{x'x''}{\lambda f}\right)\mathrm{d}x'\\ &\propto \tilde{p}(\omega - \omega_0)\exp[j(\omega - \omega_0)t_0]\\ &\quad\times\int_{x_1}w\left(x_1 - \frac{D}{2}\right)\exp\left[-j(\omega - \omega_0)\frac{\alpha x_1}{c}\right]\\ &\quad\times\int_{x_2}m\left(x_2 + \frac{D}{2}\right)\int_{x_3}\delta\left(x_3 + \frac{D}{2}\right)\\ &\quad\times\int_{x'}\exp\left[-j2\pi x'\left(\frac{x''}{\lambda f} + \frac{x_1}{\lambda f} + \frac{x_2}{\lambda_1 f} - \frac{x_3}{\lambda_1 f}\right)\right]\\ &\quad\times\mathrm{d}x'\mathrm{d}x_1\mathrm{d}x_2\mathrm{d}x_3.\end{aligned} \tag{14}$$

Integrating over the variables x', x_2, and x_3 yields

$$\begin{aligned}u_{tc2}(x'';\ \omega) &= \tilde{p}(\omega - \omega_0)\exp[j(\omega - \omega_0)t_0]\\ &\quad\times\int_{x_1}w\left(x_1 - \frac{D}{2}\right)m\left[-\frac{\lambda_1}{\lambda}(x'' + x_1)\right]\\ &\quad\times\exp\left[-j(\omega - \omega_0)\frac{\alpha x_1}{c}\right]\mathrm{d}x_1.\end{aligned} \tag{15}$$

Assuming $\Delta\lambda \ll \lambda_0$ for typical ultrashort pulses, we can also eliminate the wavelength dependence in the encoding mask by replacing λ with λ_0. It is possible to conduct the analysis without this assumption, resulting in weakly chirped output signals.[14] We next perform a change of variable by defining a new integration variable, τ, such that $x'' + x_1 = -c\tau/\alpha$. The resultant field on the grating is given by

$$\begin{aligned} u_{tc2}(x''; \omega) = {} & \tilde{p}(\omega - \omega_0)\exp[j(\omega - \omega_0)t_0] \\ & \times \exp\left[j(\omega - \omega_0)\frac{\alpha x''}{c}\right] \\ & \times \int_\tau w\left(-\frac{c}{\alpha}\tau - x'' - \frac{D}{2}\right) m\left(\frac{\lambda_1}{\lambda_0}\frac{c}{\alpha}\tau\right) \\ & \times \exp[j(\omega - \omega_0)\tau]\mathrm{d}\tau. \end{aligned} \tag{16}$$

The effect of diffraction from the output grating of the SPD is introduced into Eq. (16), yielding

$$\begin{aligned} u_{\mathrm{out}1}(x''; \omega) = {} & \tilde{p}(\omega - \omega_0)\exp[j(\omega - \omega_0)t_0] \\ & \times \exp\left\{j\left[(\omega - \omega_0)\frac{\alpha}{c} + k_g\right]x''\right\} \\ & \times \int_\tau w\left(-\frac{c}{\alpha}\tau - x'' - \frac{D}{2}\right) m\left(\frac{\lambda_1}{\lambda_0}\frac{c}{\alpha}\tau\right) \\ & \times \exp[j(\omega - \omega_0)\tau]\mathrm{d}\tau. \end{aligned} \tag{17}$$

The momentum of the diffraction grating, $k_g = \alpha\omega_0/c$, cancels the angular-dispersion term of the output field, such that all the frequency components of the short pulse copropagate at an angle θ relative to the optical axis. To propagate away from the grating plane, we reintroduce the longitudinal dependence as appears in Eq. (3) [using the local z'' coordinate (see Fig. 1) and neglecting a constant phase factor from the shift from z to z'']. We also replace the aperture function $w(\ )$ by the original spatial-mode function of the input waveform, $w_1(\ )$ [see Eq. (4)]. Additionally, we eliminate the $D/2$ shift in the pupil function, which was introduced to satisfy the phase-matching condition in the Fourier plane of the processor, yielding

$$\begin{aligned} u_{\mathrm{out}1}(x'', z'', \omega) = {} & \tilde{p}(\omega - \omega_0)\exp[j(\omega - \omega_0)t_0] \\ & \times \exp\left[j\frac{\omega}{c}(x''\sin\theta - z''\cos\theta)\right] \\ & \times \int_\tau w_1\bigg(-x''\cos\theta - z''\sin\theta \\ & - \frac{c}{\alpha}\tau\cos\theta\bigg) m\left(\frac{\lambda_1}{\lambda_0}\frac{c}{\alpha}\tau\right) \\ & \times \exp[j(\omega - \omega_0)\tau]\mathrm{d}\tau. \end{aligned} \tag{18}$$

We perform a rotation of coordinate systems from the optical system's (x'', z'') to that of the output pulse (x_2, z_2) (see Fig. 1) and take the inverse temporal FT to get the output in space–time coordinates,

$$\begin{aligned} E_{\mathrm{out}}(x_2, z_2; t) = {} & \exp\left[j\left(\frac{\omega_0}{c}z_2 - \omega_0 t\right)\right] \\ & \times \int_\tau w_1\left(-x_2 - \frac{c}{\alpha}\tau\cos\theta\right) m\left(\frac{\lambda_1}{\lambda_0}\frac{c}{\alpha}\tau\right) \\ & \times p\left(t - t_0 - \frac{z_2}{c} - \tau\right)\mathrm{d}\tau. \end{aligned} \tag{19}$$

Equation (19) describes the output temporal pulse as an integral that mixes the information from the input temporal-pulse structure, the spatially encoded mask, and the spatial-aperture function. This type of association between the spatial and temporal characteristics has been shown for other cases of ultrafast-waveform processing.[4,15,16] When the beam size of the input short-pulse signal is very narrow, the desired functionality will not be achieved. Therefore in most practical cases of interest we operate the SPD in the high-resolution limit. In this case, the spatial-mode extent (or, more precisely, time-of-flight duration) $w_1(c\tau\cos\theta/\alpha)$ is much longer than the duration of the ultrashort pulse $p(\tau)$. Thus the integral can be approximated by simply evaluating the input pupil at $\tau = t - t_0 - z_2/c$, which is the center coordinate of the short pulse $p(t)$, and taking it out of the integral, yielding

$$\begin{aligned} E_{\mathrm{out}}(x_2, z_2; t) \cong {} & \exp\left[j\left(\frac{\omega_0}{c}z_2 - \omega_0 t\right)\right] \\ & \times w_1\left[-x_2 - \frac{c}{\alpha}\cos\theta\left(t - t_0 - \frac{z_2}{c}\right)\right] \\ & \times y\left(t - t_0 - \frac{z_2}{c}\right), \end{aligned} \tag{20}$$

where $y(t)$ is defined by the convolution of the input pulse and a time-scaled encoding mask, such that

$$y(t) \equiv \int_\tau m\left(\frac{\lambda_1}{\lambda_0}\frac{c}{\alpha}\tau\right)p(t - \tau)\mathrm{d}\tau = m\left(\frac{\lambda_1}{\lambda_0}\frac{c}{\alpha}t\right) \otimes p(t). \tag{21}$$

Equation (20) describes an ultrafast waveform propagating in free space in the z_2 direction. The temporal characteristic of the output waveform, $y(t)$, is determined by the convolution operation of Eq. (21). The spatial mode of the output waveform is now space–time dependent, as is characteristic in filtering experiments of spatially dispersed temporal-frequency components.[17,18] This dependence travels along with the output waveform and represents a linear skew of the spatial mode relative to the time position of the output waveform $y(t)$. Thus there may be variations of the observed waveform at different spatial locations, a phenomenon that may influence point processes such as detection, spatial filtering, and coupling of the output signal into a single-mode fiber.

We next analyze the conversion process in the nonlinear crystal, taking into account the effect of the phase-mismatch terms of the CSN.

3. CASCADED SPATIAL–TEMPORAL WAVE MIXING

The real-time spatial–temporal wave mixing is performed by cascaded femtosecond-rate parametric interactions in a crystal exhibiting a strong $\chi^{(2)}$ coefficient. The CSN process uses a combination of frequency upconversions and frequency downconversions and has to satisfy the conditions of energy and momentum conservation for effective energy transfer. Owing to the broad temporal bandwidth of ultrashort pulses and the broad angular bandwidth of the spatial-information channel, it will be practically impossible to satisfy the phase-matching requirement necessary to achieve high conversion efficiency. Therefore nonuniform signal conversion across the temporal and spatial bandwidths will be observed, as phase matching cannot be supported in every situation. In this section we focus on the analysis of the nonlinear conversion process in the crystal.

To simplify the analysis, we assume that the generated waves in the three-wave mixing processes of the cascade are operating in the linear-conversion regime (i.e., weak interaction leading to nondepleting fundamental waves). The linear interaction allows us to decompose the waves to their temporal- and spatial-frequency domains, to treat each frequency component individually, and to integrate over the temporal and spatial bandwidths to get the output waveform. By decomposing the waves, we may use the monochromatic plane-wave solution of the wave-mixing process. The plane-wave solution will be valid as long as the nonlinear crystal is within the confocal parameter of the SDW. Since we are interested in high-resolution processing, which has a short confocal parameter, the allowable crystal length will be limited, thereby reducing the conversion efficiency. In general, there will be a trade-off between the resolution and the conversion efficiency, which is not within the scope of this study. We express the spatially and temporally decomposed input fields inside the nonlinear crystal, followed by a solution to the coupled-wave equations under the nondepleting-pump approximation. We calculate the phase-mismatch terms in the appendix.

A. Decomposed Temporal and Spatial Fields Inside the Nonlinear Birefringent Crystal

The spectrally decomposed field from the input temporal channel is found by evaluating the Fourier integral of Eq. (7), yielding

$$U_1(x';\,\omega) = \tilde{p}(\omega-\omega_0)\tilde{w}\left\{\frac{\alpha}{2\pi c}\left[\frac{\omega x'}{\alpha f} + (\omega-\omega_0)\right]\right\} \times \exp\left(-j\frac{2\pi}{\lambda}\frac{D}{2f}x'\right) \times \exp\left[-j(\omega-\omega_0)\frac{\alpha D}{2c}\right], \tag{22}$$

where the spatial FT of the input-pupil function, $\tilde{w}(\;)$, has mixed space- and temporal-frequency variables, characterizing the spatial dispersion, and we use $t_0 = \alpha D/2c$. The spatial width of $\tilde{w}$ also defines the confocal parameter, which limits our crystal length. The spatial linear phase term in Eq. (22) determines the propagation direction, owing to the spatial shift of the input pupil by $D/2$. We denote the angle between the z axis and the k vector of the propagating wave as $\theta_1 = -D/2f$, using the paraxial approximation. The SDW is incident upon the nonlinear crystal in the FT plane of the lens. At the crystal interface, located at $z' = 0$ (see Fig. 1), the wave is refracted into the crystal in accordance to Snell's law. The SDW in the crystal, when neglecting the Fresnel reflection at the boundary and accounting for field attenuation in a higher-index material, can be expressed as

$$\hat{U}_1(x';\,\omega) = \frac{\tilde{p}(\omega-\omega_0)}{\sqrt{n_o^{(\omega)}}}\tilde{w}\left\{\frac{\alpha}{2\pi c}\left[\frac{\omega x'}{\alpha f} + (\omega-\omega_0)\right]\right\} \times \exp\left(-j\frac{2\pi}{\hat{\lambda}}\frac{D}{2n_o^{(\omega)}f}x'\right) \times \exp\left[-j(\omega-\omega_0)\frac{\alpha D}{2c}\right], \tag{23}$$

where $n_o^{(\omega)}$ is the refractive index for ordinary-polarized light at frequency ω, and the hat overscript denotes variables inside the crystal (e.g., $\hat{\lambda} = \lambda/n_o^{(\omega)}$). Note that the linear phase terms of Eqs. (22) and (23) are equal in magnitude, owing to the conservation of momentum in the x' direction (i.e., kinematic condition). The propagation direction inside the crystal is frequency dependent, owing to the dispersive nature of the refractive index of the crystal.

The mask containing the spatial-domain information generates the field U_2 in the FT plane, found by evaluating the Fourier integral of Eq. (9). For the purpose of this analysis we model the spatial-information channel by $\delta(x-\xi)$, a Dirac delta function shifted from the center of the information mask by the parameter ξ. The synthesized waveform from an arbitrary mask $m(x)$ is calculated by multiplying the delta-function response by $m(\xi)$ and integrating over the parameter ξ (yielding the convolution integral). By use of the delta-function model the first input spatial channel generates an extraordinary-polarized plane wave with a single spatial frequency,

$$U_2(x',\,\xi;\,\omega_1) = \exp\left[j\frac{2\pi}{\lambda_1}\left(\frac{D}{2f} - \frac{\xi}{f}\right)x'\right]. \tag{24}$$

The angle between the z' axis and the propagation direction of this wave is denoted by $\theta_2(\xi) = (D/2-\xi)/f$. The refracted field in the crystal, $\hat{U}_2$, preserves the momentum in the x' direction and attenuates the field by the extraordinary refractive index. Evaluating the propagation angle and k vector is complicated by the refractive-index dependence on the propagation direction and is performed in the appendix.

The second spatial channel, consisting of the delta function at $x = -D/2$, generates an ordinary-polarized plane wave in the Fourier plane of the processor. Evaluating Eq. (11) and accounting for the refraction into the crystal yields

$$\hat{U}_3(x';\,\omega_1) = \frac{1}{\sqrt{n_o^{(\omega_1)}}}\exp\left(j\frac{2\pi}{\hat{\lambda}_1}\frac{D}{2n_o^{(\omega_1)}f}x'\right), \tag{25}$$

where $n_o^{(\omega_1)}$ is the ordinary refractive index at frequency ω_1. The angle between the z' axis and the propagation direction of the field before refraction is denoted by $\theta_3 = D/2f$. The nonlinear interaction of the input fields $\hat{U}_1$, $\hat{U}_2$, and $\hat{U}_3$ is analyzed next.

B. Solution of Coupled-Wave Equations Characterizing Cascaded Processes

The general solution to the coupled-mode equations governing noncollinear three-wave processes can be very complex.[19] When we limit the analysis to weak interactions with nondepleting input waves and slowly varying functions in space and time (which holds for the SDW), an analytic solution to the process is possible. Owing to the nondepleting-wave approximation, only two differential equations remain, which describe the evolution of the intermediate wave, $\hat{U}_{\text{int}}$, generated by a frequency-sum process, and the resultant output wave, $\hat{U}_4$, generated by a frequency-difference process. Geometrical factors are introduced to the coupled equations owing to the noncollinear arrangement (where we ignore the effect of the walk-off angle between the k vector and the Poynting vector in the propagation of extraordinary-polarized fields in an anisotropic crystal). We denote the angle between the z axis and the k vector of the intermediate wave as $\hat{\theta}_{\text{int}}$ and the angle between the z axis and the k vector of the output field as $\hat{\theta}_4$ (both defined inside the crystal). Both these angles vary as a function of ω and ξ (the dependence is evaluated in the appendix). Neglecting absorption in the crystal, the differential equations governing wave mixing of monochromatic plane waves are given by[20]

$$
\begin{aligned}
\frac{\mathrm{d}\hat{U}_{\text{int}}(x',\xi,z;\ \omega)}{\mathrm{d}z}
&= j\,\frac{\omega_0+\omega_1}{2\cos(\bar{\hat{\theta}}_{\text{int}})}\sqrt{\frac{\mu}{\varepsilon_{\text{int}}}}\,d\\
&\quad\times\{\hat{U}_1(x',z;\ \omega-\omega_1)\hat{U}_2(x',\xi,z;\ \omega_1)\\
&\quad\times\exp[j\Delta k^{(1)}(\omega,\xi)z]+\hat{U}_3(x',z;\ \omega_1)\\
&\quad\times\hat{U}_4(x',\xi,z;\ \omega-\omega_1)\exp[j\Delta k^{(2)}(\omega,\xi)z]\},
\end{aligned}
\tag{26a}
$$

$$
\begin{aligned}
\frac{\mathrm{d}\hat{U}_4(x',\xi,z;\ \omega)}{\mathrm{d}z}
&= j\,\frac{\omega_0}{2\cos(\bar{\hat{\theta}}_4)}\sqrt{\frac{\mu}{\varepsilon_4}}\,\mathrm{d}\hat{U}_{\text{int}}(x',\xi,z;\ \omega+\omega_1)\\
&\quad\times\hat{U}_3^{*}(x',z;\ \omega_1)\exp[-j\Delta k^{(2)}(\omega,\xi)z],
\end{aligned}
\tag{26b}
$$

where d is the second-order nonlinear optical coefficient. The right-hand side of the equations have been simplified by substituting the center-frequency value for the propagation-direction angles, $\bar{\hat{\theta}}_{\text{int}}$ and $\bar{\hat{\theta}}_4$, the electric permittivity and magnetic permeability, ε and μ, and the optical carrier in the term preceding the nonlinear polarization. The phase-mismatch terms for the frequency-sum and frequency-difference processes, $\Delta k^{(1)}(\omega,\xi)$ and $\Delta k^{(2)}(\omega,\xi)$, respectively, are given by

$$\Delta k^{(1)}(\omega,\xi)=\hat{\mathbf{k}}_1(\omega)+\hat{\mathbf{k}}_2(\xi)-\hat{\mathbf{k}}_{\text{int}}(\omega,\xi), \tag{27a}$$

$$\Delta k^{(2)}(\omega,\xi)=\hat{\mathbf{k}}_3-\hat{\mathbf{k}}_{\text{int}}(\omega,\xi)+\hat{\mathbf{k}}_4(\omega,\xi). \tag{27b}$$

Figure 2 illustrates a graphical representation of the phase-mismatch terms of Eqs. (27a) and (27b). The equations describing the phase mismatch in the wave-mixing processes are nonlinear. To simplify the phase-mismatch representation, we perform a small-signal analysis about $\omega=\omega_0$ and $\xi=0$ and linearize the relationship. The details of the linearization process and evaluation of the two phase-mismatch terms are presented in the appendix.

A simple analytic solution to the coupled differential equations can be obtained by arguing that since the generated wave $\hat{U}_4$ is weaker than the input waves, we can neglect the second nonlinear polarization term in Eq. (26a) (i.e., $\hat{U}_1\hat{U}_2 \gg \hat{U}_3\hat{U}_4$). This assumption decouples the differential equations, implying that the rate at which the intermediate wave is depleted by the second process of the cascade is much smaller than the rate at which it is being generated. Therefore Eq. (26a) of the intermediate field is dependent on the two known input fields and can be solved directly. This solution is inserted into Eq. (26b) describing the evolution of the output wave, which can also be solved directly now, as the driving waves are completely characterized. The solution yields

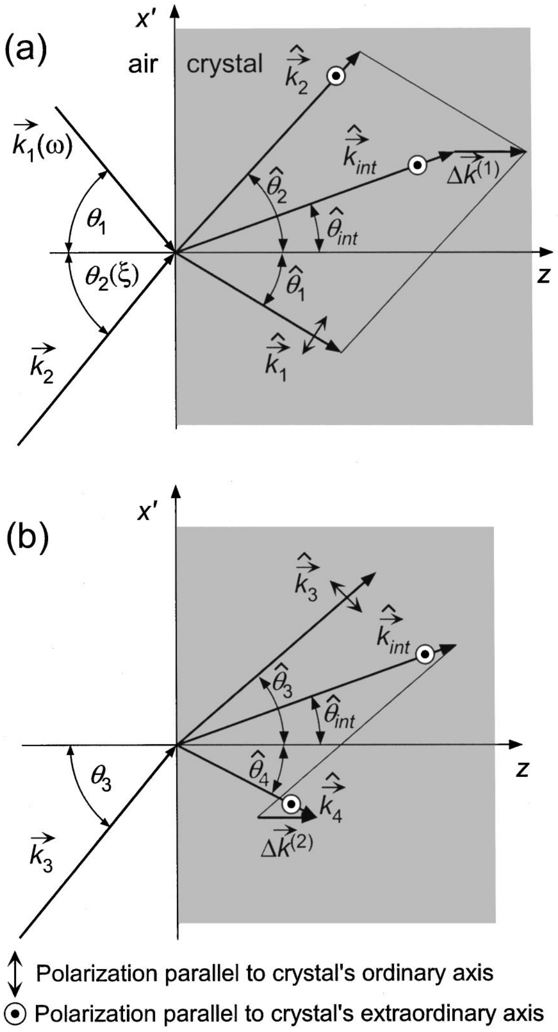

Fig. 2. Graphical representation of the phase mismatch in noncollinear mixing in an anisotropic crystal for (a) the upconversion process and (b) the downconversion process.

$$\hat{U}_4(x', \xi, z;\ \omega) \propto \hat{U}_1(x';\ \omega)\hat{U}_2(x', \xi;\ \omega_1)\hat{U}_3^*(x';\ \omega_1)H_{\mathrm{NL}}(\omega, \xi, z), \quad (28)$$

where the complex transfer function, $H_{\mathrm{NL}}(\omega, \xi, z)$, characterizes the response of the cascaded wave-mixing process and is given by

$$H_{\mathrm{NL}}(\omega, \xi, z) = \frac{\exp\{j[\Delta k^{(1)}(\omega, \xi) - \Delta k^{(2)}(\omega, \xi)]z\} - 1}{[\Delta k^{(1)}(\omega, \xi) - \Delta k^{(2)}(\omega, \xi)]\Delta k^{(1)}(\omega, \xi)} - \frac{\exp[-j\Delta k^{(2)}(\omega, \xi)z] - 1}{\Delta k^{(1)}(\omega, \xi)\Delta k^{(2)}(\omega, \xi)}. \quad (29)$$

The complex transfer function of Eq. (29) depends on the temporal-frequency component of the input pulse, on the spatial frequency arising from the amount of shift ξ of the delta function in the encoding mask, and on the length of the nonlinear crystal. Since the complex transfer function is temporal-frequency dependent, the output waveform will not be transform limited. However, any predominant quadratic-phase term can be eliminated by longitudinal adjustment of the output grating. Reintroducing the encoding-mask information, the SDW of the synthesized waveform at the edge of the crystal is defined by

$$\hat{U}_4(x', L_c;\ \omega) \propto \hat{U}_1(x';\ \omega)\hat{U}_3^*(x';\ \omega_1) \times \int_{\xi} m(\xi)\hat{U}_2(x', \xi;\ \omega_1)H_{\mathrm{NL}}(\omega, \xi, L_c)\mathrm{d}\xi, \quad (30)$$

where we replaced the interaction distance z by the thickness of the crystal, L_c. To find the output temporal waveform, Eq. (30) needs to be spatially Fourier transformed to the output plane, diffracted from the output grating, and inverse temporally Fourier transformed. Equation (30) cannot be solved analytically except for the most trivial cases, thus requiring a computation program to calculate the precise space-to-time converted waveform. Such a program could also compute the conversion efficiency, which will be information dependent.

For practical reasons it is desirable for the space-to-time processor to operate efficiently. The conversion efficiency of the wave-mixing process with CSN can be calculated with Parseval's theorem, as the total power in the spectral representation is equal to the total power in the time domain. Since Eq. (30) defines the SDW of the synthesized waveform, the power spectrum is equal to the spatial intensity distribution at the output face of the crystal. The power spectrum, or output intensity, can be evaluated analytically for a simple mask such as $m(x) = \delta(x)$, yielding

$$I_4(x';\ \omega) \propto P_1P_2P_3|\tilde{p}(\omega - \omega_0)|^2 \times \left|\tilde{w}\left\{\frac{\alpha}{2\pi c}\left[\frac{\omega x'}{\alpha f} + (\omega - \omega_0)\right]\right\}\right|^2 \times |H_{\mathrm{NL}}(\omega, 0, L_c)|^2, \quad (31)$$

where we introduce the optical powers P_1, P_2, and P_3 of the input temporal channel, the spatial-information channel, and the spatial reference channel, respectively, and

$$|H_{\mathrm{NL}}(\omega, 0, L_c)|^2 = \left(\frac{L_c}{\Delta k^{(1)}}\right)^2\Bigg(\mathrm{sinc}^2\left\{\Big[\Delta k^{(1)}(\omega, 0) - \Delta k^{(2)}(\omega, 0)\Big]\frac{L_c}{2}\right\} + \mathrm{sinc}^2\left[\Delta k^{(2)}(\omega, 0)\frac{L_c}{2}\right] - 2\,\mathrm{sinc}\left\{[\Delta k^{(1)}(\omega, 0) - \Delta k^{(2)}(\omega, 0)]\frac{L_c}{2}\right\} \times \mathrm{sinc}\left[\Delta k^{(2)}(\omega, 0)\frac{L_c}{2}\right]\cos\left[\frac{\Delta k^{(1)}(\omega, 0)L_c}{2}\right]\Bigg). \quad (32)$$

The transfer function will perform spectral filtering, as is evident from Eq. (31). The conversion efficiency, defined as the ratio of the powers of the output synthesized waveform to the input temporal channel, depends linearly on the power level of each spatial pump channel. Our findings were experimentally validated and are presented in the following section.

4. EXPERIMENTAL RESULTS OF SPACE-TO-TIME CONVERSIONS

The operation of the spatial–temporal processor of Fig. 1 was verified by synthesizing various ultrafast temporal waveforms. In the experiments we used a commercial laser system consisting of a Ti:sapphire ultrashort pulse oscillator and a regenerative amplifier. The system generates ultrashort laser pulses of 100-fs duration at a center wavelength of 800 nm with an energy level of 1 mJ per pulse. For the intense quasi-monochromatic light source required by the spatial channels we used 90% of the emitted output-pulse power and stretched the pulse to a several-picosecond duration by a grating pair. The stretched pulse was split into two beams for implementing the two quasi-monochromatic spatial channels. Since the CSN process occurs with a femtosecond-scale time response, the slow temporal-frequency variation in the stretched pulses does not affect the wave-mixing process, as long as the temporal frequencies of the two spatial channels are instantaneously equal. The remaining 10% of the short-pulse laser output power was used as the reference ultrashort pulse in the input temporal channel. The SDW U_1 is generated by a 600-lines/mm blazed grating that provides an angular-dispersion parameter of $\alpha = 0.48$ and a lens of $f = 375\,\mathrm{mm}$ focal length. The spatial–temporal wave mixing by the $\chi^{(2)}$ media was performed in a 2-mm-thick type II β-barium borate crystal. Several experiments were conducted to illustrate this real-time processing technique, demonstrating its ability to control amplitude and phase in the output temporal waveform by a complex-amplitude spatial-information channel.

All the synthesized waveforms were observed with a real-time pulse-imaging setup.[21] The pulse-imaging technique generates a spatial signal at the output plane that is proportional to the temporal convolution of the synthesized waveform and a reference ultrashort pulse. The reference-pulse source used in the pulse imager was the residual input pulse of the spatial–temporal processor, after separating it from the synthesized output waveform with a polarizing beam splitter. We viewed the output signal's intensity with a charge-coupled device and extracted the temporal information from the image.

A. Conversion Efficiency and Spectral Response

For initial characterization of the spatial–temporal wave-mixing process by CSN, the two monochromatic waves were focused by cylindrical lenses to form line sources at the input spatial channels. The resulting spatial plane waves U_2 and U_3 interact with the SDW, U_1, of an input transform-limited short pulse. Since the plane waves contain no information, in either the space or the time domain, their function is to upconvert, then downconvert, the carrier frequency of the SDW, generating by the CSN process the new SDW U_4. The downconverted SDW U_4 was generated only in the presence of the waves from the two spatial channels, verifying that the output SDW is produced by a CSN process.

The dependence of the synthesized waveform's output power to the optical power in each of the spatial channels was characterized by placing variable neutral-density filters in the spatial channels (see Fig. 3). The linear dependence of the output power to each spatial channel is verified by the excellent fit to the 10-dB/dec line. When both spatial channels' powers are varied simultaneously, the output power variation fits the 20-dB/dec line. The linear dependence confirms our assumption of the nondepleting pump approximation in Section 3. However, we observed that the dependence is sublinear when the spatial channels' powers were weak. This effect is more pronounced when only one of the spatial channels is attenuated. We believe this is due to depletion of the attenuated pump wave, as our analysis of Section 3 did not take into account strong interaction that may lead to such fundamental-wave depletion. The maximum conversion efficiency of the space-to-time processor, measured as the ratio of the input-pulse optical power to the output-pulse optical power, was 16%, illustrating the advantage of the CSN approach as opposed to conventional $\chi^{(3)}$ nonlinearity for four-wave mixing.[22]

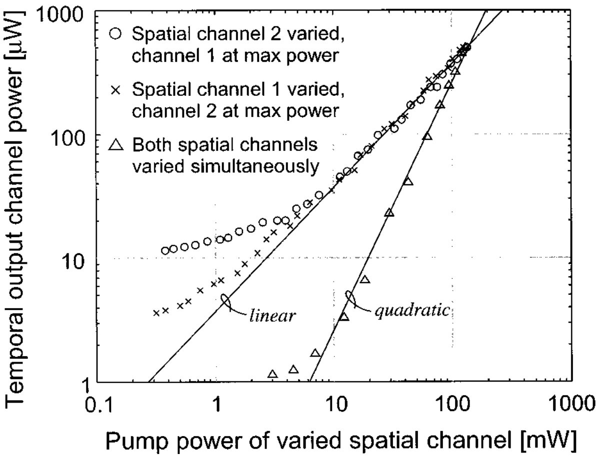

Fig. 3. Output power measurements as a function of spatial pump-beam powers. Varying one spatial channel while keeping the second constant illustrates the linear dependence of the output temporal power on each spatial channel. Varying the power of the spatial channels simultaneously displays a quadratic dependence, as expected.

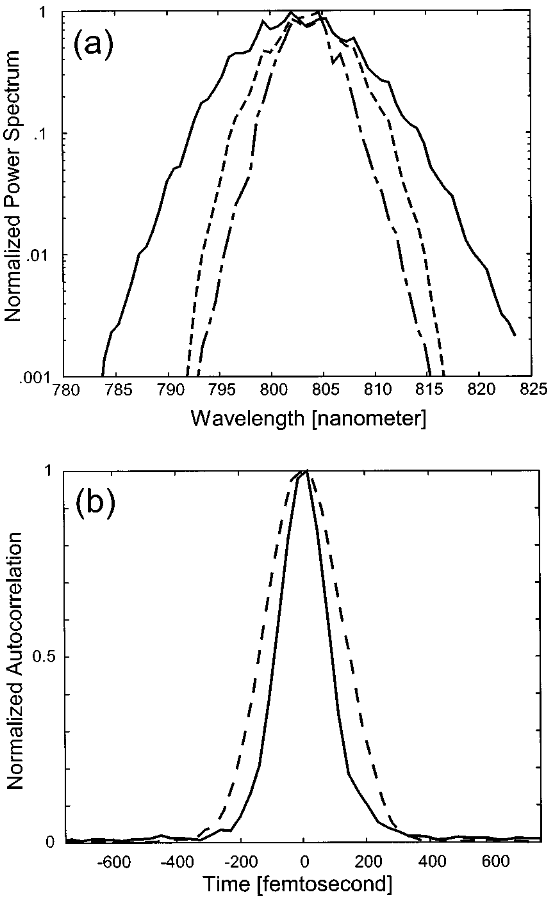

Fig. 4. (a) Measured power spectrum of the input pulse (solid curve) and the generated output pulse (dashed curve) exhibiting spectral filtering owing to a spectrally dependent phase mismatch in the processor. Also shown is the theoretical output power spectrum (dot-dash curve) calculated by applying the spectral filter to the measured input power spectrum. (b) Pulse images of the input pulse (solid curve) and the generated output pulse (dashed curve), demonstrating the increased duration of the output pulse owing to spectral filtering.

The power spectrum of the output pulse was compared with that of the input pulse (see Fig. 4a). The observed spectral narrowing is due to an increasing phase mismatch as the frequencies deviate from the center frequency. A theoretical curve of the expected output-pulse power spectrum [based on Eq. (31)] shows a close correspondence to the actual observed spectrum. The theoretical curve was generated by evaluating the phase mismatch for the two processes in the cascade with published β-barium borate parameters[23] for type II noncollinear interaction with a 4° internal angle between the fundamental waves (assuming both processes are phase matched at $\omega = \omega_0$ and $\xi = 0$). We adjusted the center frequency of the theoretical curve to match the measured data. Owing to the reduction of the available bandwidth from spectral filtering, we observed an accompanying increase in the temporal duration of the output pulse (see Fig. 4b). The measured full width at half-maximum of the detected image in the time-to-space converter increased from 182 to 288 fs.

B. Packet of Ultrafast Pulses

Novel uses for bursts of ultrashort pulses, such as terahertz-rate excitation and optical communication with ultrashort data packets, have increased the interest in developing techniques for generation of such ultrashort-pulse sequences. With the femtosecond-rate space-to-time converter, such a pulse sequence can be generated by a one-dimensional mask containing an array of point sources. The mask information can be expressed by

$$m(x) = \sum_{n=-N/2}^{N/2} A_n \delta(x - n\Delta x), \tag{33}$$

where Δx is the fixed pitch between adjacent point sources, and A_n is a scalar weight term that may be a binary bit (value of 1 or 0), a real number, or a complex number. By use of this information mask in Eq. (21), the temporal output signal takes the form

$$\begin{aligned} y(t) &= \sum_{n=-N/2}^{N/2} A_n \delta\left(t - \frac{\omega_1}{\omega_0}\frac{\alpha}{c} n\Delta x\right) \otimes p(t) \\ &= \sum_{n=-N/2}^{N/2} A_n p\left(t - \frac{\omega_1}{\omega_0}\frac{\alpha}{c} n\Delta x\right). \end{aligned} \tag{34}$$

In the space-to-time mapping, the spatial pitch Δx in the mask has been converted to a temporal separation of $\Delta t = \omega_1 \alpha \Delta x / \omega_0 c$.

Various masks containing narrow slits have been used in the space-to-time setup to generate ultrafast pulse packets. Previously, we reported results using a mask with a 0.8-mm pitch.[12] A finer mask with a 0.4-mm pitch was used to generate a denser ultrafast pulse packet (see Fig. 5). A cylindrical lenslet array was used to focus the spatial beam into the mask for increased light throughput. The spatial beam mode shape resulted in nonuniform power on each spatial slit. This power distribution has been transferred to the ultrafast pulse packet. The space-to-time mapping coefficient transforms the 0.4-mm spatial pitch to a time-domain separation of $\Delta t = 0.64$ ps (with $\omega_1 = \omega_0$ and $\alpha = 0.48$). The measured temporal separation was 0.645 ps with a resolution of 33 fs, resulting in a 1.56-THz-rate pulse packet.

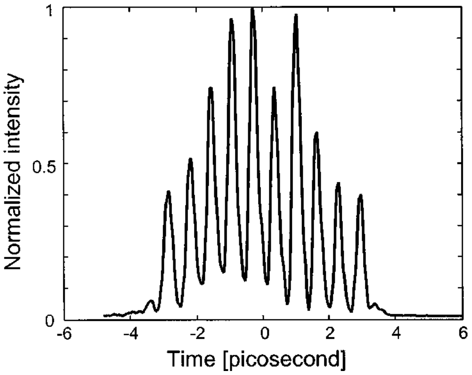

Fig. 5. 1.56-THz-rate ultrashort-pulse packet generated by a spatial-information mask consisting of a sequence of point sources separated by 0.4 mm.

C. Square Pulse

Generation of synthesized square pulses by spectral filtering is not a simple task. The mask should contain amplitude information over a wide dynamic range as well as phase information for implementing negative values. Space-to-time mapping techniques simplify the task of complex mask preparation, while the requirement for a wide dynamic range in the recording medium remains. In photorefractives, where the recorded space-charge field is dependent on the modulation function, the recording process exhibits a nonlinear dependence on the recording beams. While this enables nonlinear processing,[24] for generation of high-fidelity square pulses a weak information beam must be used, giving rise to shallow modulation depths and low diffraction efficiency.

In our wave-mixing approach with CSN the amplitude of the synthesized wave is dependent on the amplitudes of the three input waves (as long as wave depletion and phase mismatch are negligible). This linear relationship gives rise to high-fidelity conversion from space to time. In the case of a square pulse the synthesized signal may be expressed as

$$y(t) = \mathrm{rect}\left(\frac{t}{T}\right) \otimes p(t), \tag{35}$$

where $T = \omega_1 \alpha X / \omega_0 c$ is the duration of the rect function and X is the width of the slit.

An adjustable slit was placed in the spatial-information channel to experiment with several synthesized square-pulse durations. The generated waveforms (see Fig. 6) were modified in real time by changing the slit width, and the square pulses were immediately observed with the pulse imager on a monitor. At wide slit widths, nonuniformity across the top of the square pulse has been observed. We have verified that the reason is due to nonuniformity in the illumination of the spatial channel. An image of the spatial-information channel in the space-to-time processor matched well with the observed image of the synthesized waveform in the time-to-space converter. There are two limitations to the maximum slit width that can be used: the resolution of the SPD [see Eq. (19)], and the optical power from the tight focus of the spatial channel in the Fourier plane may exceed the damage threshold of the nonlinear crystal.

D. Spherical Wave Front

To demonstrate the ability to encode phase information, a point source, generated by focusing the spatial beam with a cylindrical lens, was used as the spatial-information channel. Translating the lens longitudinally away from the input plane formed a spherical wave front with variable quadratic phase on the input plane of the spatial-information channel. As the translation of the line source from the input plane is increased (in either the positive or the negative direction), the output SDW acquires a larger positive or negative quadratic phase and after recomposing on the output grating, emerges as a chirped pulse (either a positive or negative chirp). The measured synthesized chirped pulses exhibited, as expected, broader pulses along with a reduction of the peak intensity.[12]

The effect of a longitudinal translation of the point source away from the input plane of the processor is expressible as a convolution with a quadratic-phase function[25] (free space propagation), resulting in the field distribution in the spatial-information channel,

$$m(x) = \frac{\exp(jk\zeta)}{j\lambda_1\zeta}\exp\left(\frac{j\omega_1}{c}\frac{x^2}{2\zeta}\right), \qquad (36)$$

where ζ is the displacement of the focus plane of the cylindrical lens from the input plane of the processor. The phase information described in Eq. (36) gives rise to the synthesized waveform

$$y(t) = \frac{\exp(jk\zeta)}{j\lambda_1\zeta}\exp\left[\frac{j\omega_1}{c}\frac{\left(\dfrac{\omega_0 ct}{\omega_1\alpha}\right)^2}{2\zeta}\right] \otimes p(t), \qquad (37)$$

which describes a chirp function (quadratic temporal-frequency variation) imposed on the input pulse. A Fourier-domain representation of the output synthesized signal is easier to interpret in this case, yielding

$$\tilde{y}(\omega) \propto \exp\left[-j\left(\frac{\omega-\omega_0}{\omega_0}\right)^2\frac{\omega_1\zeta\alpha^2}{c}\right]\tilde{p}(\omega-\omega_0). \qquad (38)$$

From Eq. (38) it is clear that the amount of chirp is linearly dependent on the displacement ζ.

To measure the amount of chirp that is present in the synthesized waveform, we utilize a unique property of the pulse imager. Since the pulse imager generates the complex-amplitude information of the temporal convolution operation in spatial coordinates, the resulting spatial quadratic phase in the image of a chirped pulse can be used to gauge the amount of chirp. By longitudinally translating the output plane, a location can be found where the wave focuses to its tightest spot size, eliminating the spatial quadratic phase.[21] Therefore as the pulse chirp is increased (either positively or negatively), the location of the plane at which the wave focuses changes (either farther or closer). The spatial output signal of the pulse imager can be expressed as[21]

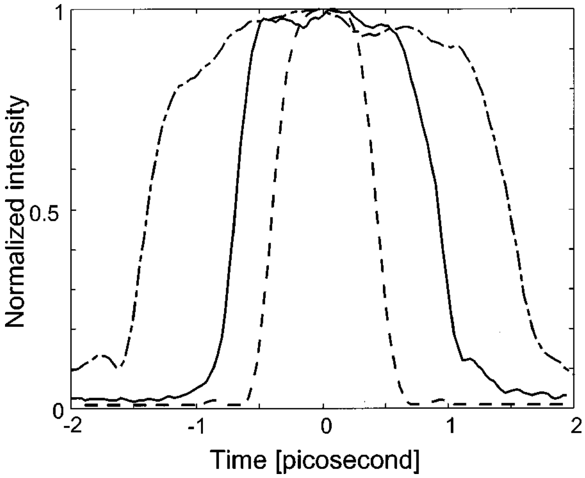

Fig. 6. Superimposed images of square pulses generated by varying the width of a square aperture in the spatial channel.

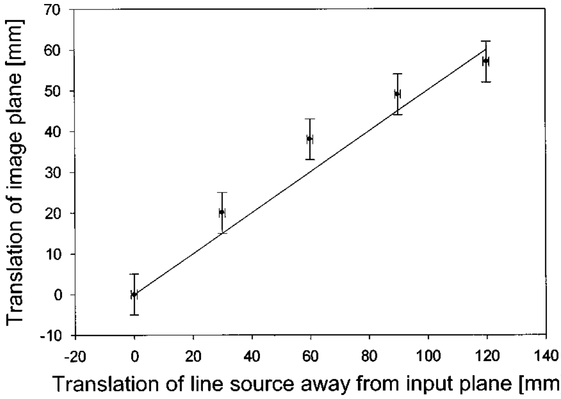

Fig. 7. Linear correspondence between translation of the point source away from the input plane of space-to-time converter and translation of the image-formation plane in the pulse imager. The solid line corresponds to a theoretical curve of slope 1/2.

$$\begin{aligned} b(x'') &= p\left(\frac{2\alpha}{c}x''\right) \otimes y\left(-\frac{2\alpha}{c}x''\right) \\ &= p\left(\frac{2\alpha}{c}x''\right) \otimes p\left(-\frac{2\alpha}{c}x''\right) \\ &\quad \otimes \exp\left[\frac{j\omega_1}{c}\frac{\left(\dfrac{\omega_0}{\omega_1}2x''\right)^2}{2\zeta}\right], \end{aligned} \qquad (39)$$

which corresponds to the convolution of the ultrashort pulses with a quadratic-phase function. Using the kernel of free-space propagation at frequency $2\omega_0$, $\exp[j(2\omega_0/c)(x''^2/2Z)]$, where Z is the displacement from the image plane, we seek the value of Z that will cancel the quadratic-phase terms in Eq. (39). This value of Z corresponds to the location where the signal focuses to its tightest spot size. The value of Z is given by

$$Z = -\frac{\omega_1}{\omega_0}\frac{\zeta}{2}. \qquad (40)$$

This scaling rule is dependent on the ratio of the frequencies used in the spatial and temporal channels of the space-to-time converter and a factor of 2 owing to the doubled-frequency output of the pulse imager.

We have verified experimentally the relation in Eq. (40) by finding the location where the output of the pulse imager focuses, for each translated location used in the spatial channel of the space-to-time converter (see Fig. 7). In our experiment the scaling rule reduces to 1/2 since $\omega_1 = \omega_0$. Thus we have a correspondence between the longitudinal translation of the line source in the input spatial channel of the spatial–temporal processor and the longitudinal translation of the focus plane of the pulse imager.

5. CONCLUSION AND DISCUSSION

We have introduced and experimentally demonstrated femtosecond-rate space-to-time conversion of amplitude and phase information from a quasi-monochromatic spatial-image channel to an ultrafast temporal waveform. Relative to other spatial–temporal processing techniques, the CSN four-wave mixing approach provides femtosecond-rate processing owing to the fast bound-electron nonlinearity and high efficiency on account of a relatively large $\chi^{(2)}$ coefficient. Such capabilities are required for quantum control experiments or ultrafast data modulation in optical communications, where rapid, high-fidelity waveform manipulations are required.

To model limitations imposed by phase-matching considerations in the nonlinear wave-mixing process, we have introduced a complex transfer function to characterize the system response. The phase mismatch in the wave-mixing process arises from the broad temporal- and spatial-frequency content of the input temporal-pulse and spatial-image information, respectively. The transfer function can be used to compute the precise space-to-time converted waveform and assist in optimal selection of a nonlinear crystal for real-time pulse shaping. The conversion efficiency from the input reference pulse to the output synthesized waveform was found to depend on the power levels of the two spatial channels.

Several experiments were conducted to illustrate the ability to convert amplitude and phase information from the space domain to the time domain with high efficiency. The spectrum reduction in the synthesized waveform owing to the complex transfer function was observed and was in good agreement with the predicted spectrum. All the experiments were conducted on a single-shot basis, highlighting the benefit of processing with a fast nonlinear effect.

The space-to-time conversion process that we have demonstrated uses an identical quasi-monochromatic light source in the two spatial channels. This requirement is typical for holographic processing, where the two waves need to be mutually coherent during the long recording phase. Since our processor is based on a real-time four-wave mixing process, this requirement can be alleviated. The necessary condition for a faithful signal conversion by nonlinear wave mixing is that each of the spatial channels be implemented with a monochromatic light source, with no temporal bandwidth. With this condition the nonlinear polarization term can be trivially calculated [as we have done in Eqs. (12) and (13)]. It is therefore feasible to perform wavelength tuning of the synthesized temporal waveform by use of different optical frequencies in the two spatial channels. The center frequency of the synthesized temporal waveform is shifted by the frequency difference of the two sources used in the spatial channels. Since quasi-monochromatic light sources are used in reality, we require that the coherence time of the light sources be much longer than the time window of the SPD (which is a very simple requirement to satisfy). The propagation directions of the fields from the two spatial channels may require adjustment, such that the phase-matching condition is satisfied for the two processes of the cascade. The hypothesized wavelength-tuning property of the real-time four-wave mixing processor is unique to our space-to-time technique and cannot be accomplished by holographic recording means.

APPENDIX A: EVALUATION OF PHASE-MISMATCH TERMS

The output signal of the CSN process was shown in Subsection 3.B to depend on the phase-mismatch terms in the coupled-wave equations characterizing the generation of the new fields. The phase mismatch occurs since the phase-matching requirement for efficient energy transfer cannot be supported for the temporal bandwidth of the SDW and the angular bandwidth of the spatial-information channel. In this appendix we derive the phase-mismatch terms for the two processes of the cascade, using the information-channel model of a delta function shifted by an amount ξ. The phase-mismatch terms obtained in this appendix are inserted into Eq. (29), describing the complex transfer function of the processor.

The first nonlinear interaction of the cascade, the frequency-sum process, generates the intermediate wave, $\hat{U}_{\mathrm{int}}$. (Note that all properties of the waves inside the crystal are with the hat overscript.) The phase mismatch of the first process of the cascade is defined by the vector equation, Eq. (27a), where the phase mismatch must lie in the z direction owing to the kinematic condition (conservation of momentum in the x' direction). Since the interacting waves are propagating at very small angles relative to the z axis, we can use the paraxial approximation (note that Fig. 2 shows greatly exaggerated angles), simplifying the phase-mismatch expression to the sum of the k-vector magnitudes, i.e., $\Delta k^{(1)}(\omega, \xi) \cong \hat{k}_1(\omega) + \hat{k}_2(\xi) - \hat{k}_{\mathrm{int}}(\omega, \xi)$. We next find these k-vector magnitudes for evaluation of the first phase-mismatch term.

The first input wave, $\hat{U}_1$, from the input temporal channel, is polarized parallel to the crystal's ordinary axis. Therefore the wave-vector magnitude is independent of its propagation direction and is given by $\hat{k}_1(\omega) \approx k(\omega_0) + (\partial k/\partial \omega)(\omega - \omega_0)$. To find the wave-vector magnitude of the intermediate wave, $\hat{U}_{\mathrm{int}}$, and its propagation direction, we apply the kinematic condition using the paraxial approximation, yielding

$$\begin{aligned}\hat{k}_{\mathrm{int}}(\omega, \xi)\hat{\theta}_{\mathrm{int}}(\omega, \xi) &= \hat{k}_1(\omega)\hat{\theta}_1(\omega) + \hat{k}_2(\xi)\hat{\theta}_2(\xi)\\ &= k_1(\omega)\theta_1 + k_2\theta_2(\xi),\end{aligned} \tag{A1}$$

where the second equality results from invoking the kinematic condition on the input fields across the crystal interface. (Before refraction into the crystal, θ_1 is not frequency dependent, as all the components propagate in the same direction [see Eq. (22)], and the magnitude of k_2 does not vary with the shift of in ξ, as it is a quasi-monochromatic wave.) To analyze the effect of varying the parameters $\Delta\omega = \omega - \omega_0$ and ξ, we perform a small-signal perturbation about $\omega = \omega_0$ and $\xi = 0$ by defining the following:

$$\hat{k}_{\mathrm{int}}(\omega, \xi) = \bar{\hat{k}}_{\mathrm{int}} + \Delta\hat{k}_{\mathrm{int}},$$

$$\hat{\theta}_{\mathrm{int}}(\omega, \xi) = \bar{\hat{\theta}}_{\mathrm{int}} + \Delta\hat{\theta}_{\mathrm{int}},$$

$$k_1(\omega) = \frac{\omega_0}{c} + \frac{\Delta\omega_0}{c},$$

$$\theta_2(\xi) = \frac{D}{2f} - \frac{\xi}{f}, \tag{A2}$$

where $\bar{\hat{k}}_{\text{int}}$ and $\bar{\hat{\theta}}_{\text{int}}$ are the k-vector magnitude and angle of propagation, respectively, for the intermediate wave evaluated at $\omega = \omega_0$ and $\xi = 0$. Inserting the perturbed expressions into Eq. (A1), neglecting second-order terms of the form $\Delta\hat{k}_{\text{int}}\Delta\hat{\theta}_{\text{int}}$, and simplifying the expression by removing the constant terms that satisfy the equality on both sides of the equation yields

$$\Delta\hat{k}_{\text{int}}\bar{\hat{\theta}}_{\text{int}} + \bar{\hat{k}}_{\text{int}}\Delta\hat{\theta}_{\text{int}} = -\frac{D}{2f}\frac{\Delta\omega}{c} - \frac{\omega_1}{c}\frac{\xi}{f}, \tag{A3}$$

where we used $\theta_1 = -D/2f$ and $k_2 = \omega_1/c$. We can further simplify the expression by setting $\Delta\hat{k}_{\text{int}} = (\partial\hat{k}_{\text{int}}/\partial\omega)\Delta\omega + (\partial\hat{k}_{\text{int}}/\partial\theta)\Delta\hat{\theta}_{\text{int}}$, resulting in

$$\Delta\hat{\theta}_{\text{int}} = -\frac{\dfrac{D}{2fc} + v_{g\_\text{int}}^{-1}\bar{\hat{\theta}}_{\text{int}}}{\dfrac{\partial\hat{k}_{\text{int}}}{\partial\theta}\bar{\hat{\theta}}_{\text{int}} + \bar{\hat{k}}_{\text{int}}}\Delta\omega - \frac{\dfrac{\omega_1}{cf}}{\dfrac{\partial\hat{k}_{\text{int}}}{\partial\theta}\bar{\hat{\theta}}_{\text{int}} + \bar{\hat{k}}_{\text{int}}}\xi, \tag{A4}$$

where we used the definition of the group velocity, $v_{g\_\text{int}} = (\partial\hat{k}_{\text{int}}/\partial\omega)^{-1}$. Using this result, we can express the k vector of the intermediate wave as

$$\hat{k}_{\text{int}}(\omega, \xi) = \bar{\hat{k}}_{\text{int}} + \left(v_{g\_\text{int}}^{-1} - \frac{\partial\hat{k}_{\text{int}}}{\partial\theta}\frac{\dfrac{D}{2fc} + v_{g\_\text{int}}^{-1}\bar{\hat{\theta}}_{\text{int}}}{\dfrac{\partial\hat{k}_{\text{int}}}{\partial\theta}\bar{\hat{\theta}}_{\text{int}} + \bar{\hat{k}}_{\text{int}}}\right) \times (\omega - \omega_0) - \frac{\dfrac{\partial\hat{k}_{\text{int}}}{\partial\theta}\dfrac{\omega_1}{c}}{\dfrac{\partial\hat{k}_{\text{int}}}{\partial\theta}\bar{\hat{\theta}}_{\text{int}} + \bar{\hat{k}}_{\text{int}}}\frac{\xi}{f}. \tag{A5}$$

The term $\partial\hat{k}_{\text{int}}/\partial\theta$ is evaluated by $[(\omega_0 + \omega_1)/c] \times (\partial n_e^{(\omega_0+\omega_1)}/\partial\theta)$, where the rate of change of the extraordinary refractive index at angle $\bar{\hat{\theta}}_{\text{int}}$ can be found by differentiating the equation governing the refractive-index dependence on angle θ of an anisotropic crystal.[26]

Next, we find the k-vector properties of the wave from the spatial-information channel, $\hat{U}_2$, which is also polarized in the direction of the extraordinary axis. Since this wave is quasimonochromatic, the propagation direction inside the crystal determines the wave-vector magnitude. We find the propagation direction by using the kinematic condition across the crystal interface together with a small-signal perturbation, yielding

$$\begin{aligned}\hat{k}_2(\hat{\theta}_2)\hat{\theta}_2 &= \frac{\omega_1}{c}n_e^{(\omega_1)}[\hat{\theta}_2(\xi)]\hat{\theta}_2(\xi)\\ &\cong \frac{\omega_1}{c}(n_2 + \Delta n_2)(\bar{\hat{\theta}}_2 + \Delta\hat{\theta}_2)\\ &= \frac{\omega_1}{c}\left(\frac{D}{2f} - \frac{\xi}{f}\right),\end{aligned} \tag{A6}$$

where $\bar{\hat{\theta}}_2$ is the angle between the propagation direction and the z axis for no spatial shift of the delta function. By neglecting second-order terms of the form $\Delta n_2\Delta\hat{\theta}_2$, and expressing the index change as $\Delta n_2 = (\mathrm{d}n_e^{(\omega_1)}/\mathrm{d}\theta)\Delta\hat{\theta}_2$, we find

$$\Delta\hat{\theta}_2 = \frac{-\dfrac{\xi}{f}}{n_2 + \bar{\hat{\theta}}_2\left.\dfrac{\mathrm{d}n_e^{(\omega_1)}}{d\theta}\right|_{\theta=\bar{\hat{\theta}}_2}}, \tag{A7}$$

where the derivative of the refractive index can again be calculated.[26] The k vector of the field is given by $\omega_1(n_2 + \Delta n_2)/c$, yielding

$$k_2(\xi) \cong \frac{\omega_1}{c}n_e^{(\omega_1)}(\bar{\hat{\theta}}_2) + \frac{\omega_1}{c}\left.\frac{\mathrm{d}n_e^{(\omega_1)}}{\mathrm{d}\theta}\right|_{\theta=\bar{\hat{\theta}}_2} \times \frac{-\dfrac{\xi}{f}}{n_e^{(\omega_1)}(\bar{\hat{\theta}}_2) + \bar{\hat{\theta}}_2\left.\dfrac{\mathrm{d}n_e^{(\omega_1)}}{\mathrm{d}\theta}\right|_{\theta=\bar{\hat{\theta}}_2}}. \tag{A8}$$

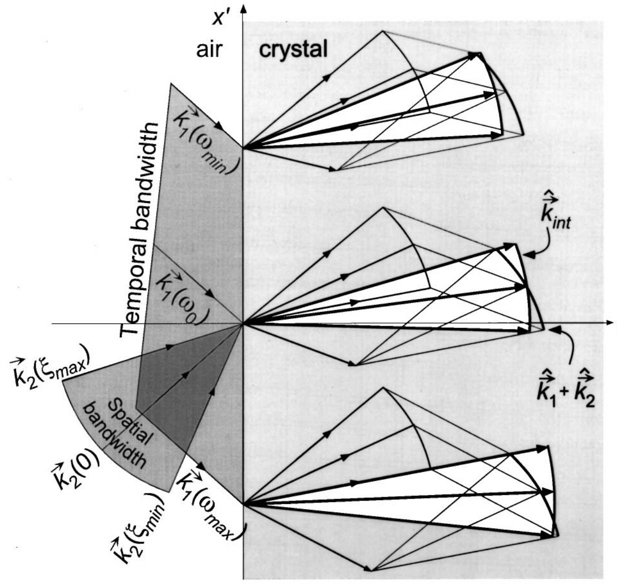

Fig. 8. Illustration of phase mismatch owing to broad temporal bandwidth (spatially dispersed along x') and angular bandwidth. The vector sum of the two fundamental waves generates a k-vector front that is compared with the available k-vector front of the frequency-sum wave. Exact phase matching is possible at each temporal frequency with different components of the spatial angular bandwidth.

The phase mismatch of the first process of the cascade is therefore found by combining the expressions for the wave-vector magnitudes, resulting in

$$
\begin{aligned}
\Delta k^{(1)}(\omega, \xi)
&= \hat{k}_1(\omega) + \hat{k}_2(\xi) - \hat{k}_{\mathrm{int}}(\omega, \xi) \\
&= \left[\frac{\omega_0}{c} n_o^{(\omega_0)} + \frac{\omega_1}{c} n_e^{(\omega_1)}(\bar{\hat{\theta}}_2) - \frac{\omega_0 + \omega_1}{c} n_e^{(\omega_0+\omega_1)}(\bar{\hat{\theta}}_{\mathrm{int}})\right] \\
&\quad + \left(\nu_{g\_1}^{-1} - \nu_{g\_\mathrm{int}}^{-1} + \frac{\partial \hat{k}_{\mathrm{int}}}{\partial \theta} \frac{\dfrac{D}{2fc} + \nu_{g\_\mathrm{int}}^{-1} \bar{\hat{\theta}}_{\mathrm{int}}}{\dfrac{\partial \hat{k}_{\mathrm{int}}}{\partial \theta} \bar{\hat{\theta}}_{\mathrm{int}} + \bar{\hat{k}}_{\mathrm{int}}} \right) \\
&\quad \times (\omega - \omega_0) + \left[\frac{ -\dfrac{\omega_1}{c} \left.\dfrac{\mathrm{d}n_e^{(\omega_1)}}{\mathrm{d}\theta}\right|_{\theta=\bar{\hat{\theta}}_2} }{ n_e^{(\omega_1)}(\bar{\hat{\theta}}_2) + \bar{\hat{\theta}}_2 \left.\dfrac{\mathrm{d}n_e^{(\omega_1)}}{\mathrm{d}\theta}\right|_{\theta=\bar{\hat{\theta}}_2} } \right. \\
&\quad \left. + \frac{ \dfrac{\partial \hat{k}_{\mathrm{int}}}{\partial \theta} \dfrac{\omega_1}{c} }{ \dfrac{\partial \hat{k}_{\mathrm{int}}}{\partial \theta} \bar{\hat{\theta}}_{\mathrm{int}} + \bar{\hat{k}}_{\mathrm{int}} } \right] \frac{\xi}{f} \\
&\equiv \Delta k^{(1)}(\omega_0, 0) + \frac{\partial \Delta k^{(1)}}{\partial \omega}(\omega - \omega_0) + \frac{\partial \Delta k^{(1)}}{\partial \xi}\xi. \qquad \text{(A9)}
\end{aligned}
$$

The constant term of the phase mismatch is set to zero by proper crystal selection, cut, and orientation set to satisfy the phase-matching condition for the center frequency ω_0 and without spatial offset ξ. Figure 8 graphically illustrates the difference between the vector sum of $\hat{k}_1(\omega)$ (spatially dispersed in the x' direction) and $\hat{k}_2(\xi)$ (broad spatial bandwidth at every location) and $\hat{k}_{\mathrm{int}}(\omega, \xi)$ (available wave vectors that the crystal supports).

The calculation of the phase-mismatch term is repeated for the second interaction of the cascade, the frequency-difference process, which generates the output wave, $\hat{U}_4$. By reasoning of the paraxial approximation the phase mismatch of the second process of the cascade is again an equation with wave-vector magnitudes, i.e., $\Delta k^{(2)}(\omega, \xi) = \hat{k}_3 + \hat{k}_4(\omega, \xi) - \hat{k}_{\mathrm{int}}(\omega, \xi)$. The magnitude of the wave vector from the second spatial channel is $\omega_1 n_o^{(\omega_1)}/c$, as the quasi-monochromatic wave is polarized in the direction of the crystal's ordinary axis. The wave-vector properties of the output wave are calculated with the kinematic condition, yielding

$$
\begin{aligned}
\hat{k}_4(\omega, \xi)\hat{\theta}_4(\omega, \xi) &= \hat{k}_{\mathrm{int}}(\omega, \xi)\hat{\theta}_{\mathrm{int}}(\omega, \xi) - \hat{k}_3\theta_3 \\
&= k_1(\omega)\theta_1 + k_2\theta_2(\xi) - k_3\theta_3, \qquad \text{(A10)}
\end{aligned}
$$

where Eq. (A1) was used to simplify the expression. A small-signal perturbation about $\omega = \omega_0$ and $\xi = 0$ is performed on Eq. (A10) to analyze the effect of the temporal and angular bandwidths. Using $\Delta\hat{k}_4 = (\partial\hat{k}_4/\partial\omega)\Delta\omega + (\partial\hat{k}_4/\partial\theta)\Delta\hat{\theta}_4$, neglecting second-order terms of the form $\Delta\hat{k}_4\Delta\hat{\theta}_4$, and simplifying the resulting expression, we obtain

$$
\Delta\hat{\theta}_4 = -\frac{\dfrac{D}{2fc} + v_{g\_4}^{-1}\bar{\hat{\theta}}_4}{\dfrac{\partial\hat{k}_4}{\partial\theta}\bar{\hat{\theta}}_4 + \bar{\hat{k}}_4}\Delta\omega - \frac{\dfrac{\omega_1}{c}}{\dfrac{\partial\hat{k}_4}{\partial\theta}\bar{\hat{\theta}}_4 + \bar{\hat{k}}_4}\frac{\xi}{f}. \qquad \text{(A11)}
$$

The similarity between the expressions describing the perturbation angles $\Delta\hat{\theta}_{\mathrm{int}}$ and $\Delta\hat{\theta}_4$ [Eqs. (A4) and (A11)] arises from the identical dependence on the variational parameters on the right-hand sides of Eqs. (A1) and (A10). The wave-vector magnitude of the output field is expressed by

$$
\begin{aligned}
\hat{k}_4(\omega, \xi) &= \bar{\hat{k}}_4 + \left(v_{g\_4}^{-1} - \frac{\partial\hat{k}_4}{\partial\theta} \frac{\dfrac{D}{2fc} + v_{g\_4}^{-1}\bar{\hat{\theta}}_4}{\dfrac{\partial\hat{k}_4}{\partial\theta}\bar{\hat{\theta}}_4 + \bar{\hat{k}}_4} \right)(\omega - \omega_0) \\
&\quad - \frac{\dfrac{\partial\hat{k}_4}{\partial\theta}\dfrac{\omega_1}{c}}{\dfrac{\partial\hat{k}_4}{\partial\theta}\bar{\hat{\theta}}_4 + \bar{\hat{k}}_4}\frac{\xi}{f}. \qquad \text{(A12)}
\end{aligned}
$$

The phase mismatch of the second process of the cascade is therefore given by

$$
\begin{aligned}
\Delta k^{(2)}(\omega, \xi)
&= \hat{k}_3 + \hat{k}_4(\omega, \xi) - \hat{k}_{\mathrm{int}}(\omega, \xi) \\
&= \left[\frac{\omega_1}{c} n_0^{(\omega_1)} + \frac{\omega_0}{c} n_e^{(\omega_0)}(\bar{\hat{\theta}}_4) - \frac{\omega_0 + \omega_1}{c} n_e^{(\omega_0+\omega_1)}(\bar{\hat{\theta}}_{\mathrm{int}})\right] \\
&\quad + \left(v_{g\_4}^{-1} - v_{g\_\mathrm{int}}^{-1} + \frac{\partial\hat{k}_{\mathrm{int}}}{\partial\theta} \frac{\dfrac{D}{2fc} + v_{g\_\mathrm{int}}^{-1}\bar{\hat{\theta}}_{\mathrm{int}}}{\dfrac{\partial\hat{k}_{\mathrm{int}}}{\partial\theta}\bar{\hat{\theta}}_{\mathrm{int}} + \bar{\hat{k}}_{\mathrm{int}}} \right. \\
&\quad \left. - \frac{\partial\hat{k}_4}{\partial\theta} \frac{\dfrac{D}{2fc} + v_{g\_4}^{-1}\bar{\hat{\theta}}_4}{\dfrac{\partial\hat{k}_4}{\partial\theta}\bar{\hat{\theta}}_4 + \bar{\hat{k}}_4} \right)(\omega - \omega_0) \\
&\quad + \left(\frac{\dfrac{\partial\hat{k}_{\mathrm{int}}}{\partial\theta}\dfrac{\omega_1}{c}}{\dfrac{\partial\hat{k}_{\mathrm{int}}}{\partial\theta}\bar{\hat{\theta}}_{\mathrm{int}} + \bar{\hat{k}}_{\mathrm{int}}} - \frac{\dfrac{\partial\hat{k}_4}{\partial\theta}\dfrac{\omega_1}{c}}{\dfrac{\partial\hat{k}_4}{\partial\theta}\bar{\hat{\theta}}_4 + \bar{\hat{k}}_4} \right)\frac{\xi}{f} \\
&\equiv \Delta k^{(2)}(\omega_0, 0) + \frac{\partial\Delta k^{(2)}}{\partial\omega}(\omega - \omega_0) + \frac{\partial\Delta k^{(2)}}{\partial\xi}\xi. \qquad \text{(A13)}
\end{aligned}
$$

The constant term of the phase mismatch in the second process can be shown to be nonzero by use of the phase-matching condition from the first process of the cascade. The resulting constant phase mismatch is given by

$$\Delta k^{(2)}(\omega_0, 0) = \frac{\omega_0}{c}[n_e^{(\omega_0)}(\bar{\hat{\theta}}_4) - n_o^{(\omega_0)}] - \frac{\omega_1}{c}[n_e^{(\omega_1)}(\bar{\hat{\theta}}_2) - n_o^{(\omega_1)}]. \quad \text{(A14)}$$

The phase mismatch is caused by the crystal's birefringence. The two quasi-monochromatic spatial waves, which copropagate in free space, have different propagation directions inside the crystal since each wave experiences a different refractive index. Therefore the second process cannot be phase matched for the center temporal- and spatial-frequency components. However, the location of the point source in the second spatial input channel [see Eq. (10)] can be slightly shifted in experiment from $-D/2$, such that the second process is also phase matched and high conversion efficiency is achieved. This results in a small propagation-angle offset between the residual wave U_1 and the output wave U_4, which is expected owing to the kinematic condition and was observed in our experiments.

Evaluation of the various propagation angles inside the crystal and the crystal properties at these angles are required for determining $\Delta k^{(1)}$ and $\Delta k^{(2)}$, which are used in conjunction with the nonlinear conversion analysis of Section 3.

ACKNOWLEDGMENTS

This work was supported in part by the Ballistic Missile Defense Organization, the U.S. Air Force Office of Scientific Research, and the National Science Foundation. Dan Marom and Dmitriy Panasenko gratefully acknowledge the support of the Fannie and John Hertz foundation.

*Curent address: Lucent Technologies, Room 4B-411, 101 Crawfords Corner Road, Holmdel, New Jersey 07733.

REFERENCES

1. C. Froehly, B. Colombeau, and M. Vampouille, "Shaping and analysis of picosecond light pulses," in *Progress in Optics XX*, E. Wolf, ed. (North-Holland, Amsterdam, 1983), pp. 65–153.
2. A. M. Weiner, "Femtosecond optical pulse shaping and processing," Prog. Quantum Electron. **19**, 161–237 (1995).
3. Y. T. Mazurenko, "Holography of wave packets," Appl. Phys. B **50**, 101–114 (1990).
4. A. M. Weiner, J. P. Heritage, and E. M. Kirschner, "High-resolution femtosecond pulse shaping," J. Opt. Soc. Am. B **5**, 1563–1572 (1988).
5. A. M. Weiner, D. E. Leaird, J. S. Patel, and J. R. Wullert, "Programmable femtosecond pulse shaping by use of a multielement liquid-crystal phase modulator," Opt. Lett. **15**, 326–328 (1990).
6. M. E. Fermann, V. di Silva, D. A. Smith, Y. Silberberg, and A. M. Weiner, "Shaping of ultrashort optical pulses by using an integrated acousto-optic tunable filter," Opt. Lett. **18**, 1505–1507 (1993).
7. M. M. Wefers and K. A. Nelson, "Programmable phase and amplitude femtosecond pulse shaping," Opt. Lett. **18**, 2032–2034 (1993).
8. M. C. Nuss and R. L. Morrison, "Time-domain images," Opt. Lett. **20**, 740–742 (1995).
9. P. C. Sun, Y. Mazurenko, W. S. C. Chang, P. K. L. Yu, and Y. Fainman, "All-optical parallel-to-serial conversion by holographic spatial-to-temporal frequency encoding," Opt. Lett. **20**, 1728–1730 (1995).
10. M. C. Nuss, M. Li, T. H. Chiu, A. M. Weiner, and A. Partovi, "Time-to-space mapping of femtosecond pulses," Opt. Lett. **19**, 664–666 (1994).
11. Y. Ding, R. M. Brubaker, D. D. Nolte, M. R. Melloch, and A. M. Weiner, "Femtosecond pulse shaping by dynamic holograms in photorefractive multiple quantum wells," Opt. Lett. **22**, 718–720 (1997).
12. D. M. Marom, D. Panasenko, P.-C. Sun, and Y. Fainman, "Spatial-temporal wave mixing for space-to-time conversion," Opt. Lett. **24**, 563–565 (1999).
13. M. A. Krumbügel, J. N. Sweetser, D. N. Fittinghoff, K. W. DeLong, and R. Trebino, Opt. Lett. **22**, 245–247 (1997).
14. D. M. Marom, P. C. Sun, and Y. Fainman, "Analysis of spatial-temporal converters for all-optical communication links," Appl. Opt. **37**, 2858–2868 (1998).
15. O. E. Martinez, "Grating and prism compressors in the case of finite beam size," J. Opt. Soc. Am. B **3**, 929–934 (1986).
16. M. M. Wefers and K. A. Nelson, "Analysis of programmable ultrashort waveform generation using liquid-crystal spatial light modulators," J. Opt. Soc. Am. B **12**, 1343–1362 (1995).
17. J. Paye and A. Migus, "Space–time Wigner functions and their applications to the analysis of a pulse shaper," J. Opt. Soc. Am. B **12**, 1480–1490 (1995).
18. M. M. Wefers and K. A. Nelson, "Space–time profiles of shaped ultrafast optical waveforms," IEEE J. Quantum Electron. **32**, 161–172 (1996).
19. Y. R. Shen, *The Principles of Nonlinear Optics* (Wiley, New York, 1984), Chap. 6.
20. M. Schubert and B. Wilhelmi, *Nonlinear Optics and Quantum Electronics* (Wiley, New York, 1986), Chap. 1.
21. P. C. Sun, Y. T. Mazurenko, and Y. Fainman, "Femtosecond pulse imaging: ultrafast optical oscilloscope," J. Opt. Soc. Am. A **14**, 1159–1170 (1997).
22. J. B. Khurgin, A. Obeidat, S. J. Lee, and Y. J. Ding, "Cascaded optical nonlinearities: microscopic understanding as a collective effect," J. Opt. Soc. Am. B **14**, 1977–1983 (1997).
23. V. G. Dmitriev, G. G. Gurzadyan, and D. N. Nikogosyan, *Handbook of Nonlinear Optical Crystals*, 2nd ed. (Springer-Verlag, Berlin, 1997).
24. Y. Ding, D. D. Nolte, M. R. Melloch, and A. M. Weiner, "Time-domain image processing using dynamic holography," IEEE J. Sel. Top. Quantum Electron. **4**, 332–341 (1998).
25. J. W. Goodman, *Introduction to Fourier Optics*, 2nd ed. (McGraw-Hill, New York, 1996), Chap. 4.
26. A. Yariv and P. Yeh, *Optical Waves in Crystals* (Wiley, New York, 1984), Chap. 12.